

FINAL DEGREE PROJECT

Design of infrared filters to improve the quality of a
superconducting qubit

Santiago Vallés Sanclemente

Supervised by:

Dr. Pol Forn-Díaz (BSC-IFAE)

Dr. Gemma Rius Suñé (IMB-CNM-CSIC)

Degree in Physics

Bellaterra, 17th of June, 2019



Contents

1	Introduction	2
2	Basics of quantum computation	3
2.1	Superconducting qubits and Josephson Junctions	4
2.2	Noise sources and how to reduce their impact	6
3	Computational simulation	9
3.1	Capacitance matrix of a Josephson Junction	9
3.2	Resonant modes of a 3D cavity	11
4	Filtering with an epoxy coating	14
4.1	Previous works	14
4.2	Design and fabrication process	15
4.3	Filter characterisation	16
4.4	Epoxy absorption analysis	17
5	Conclusions	23
	Bibliography	26
	Appendix A Simulation workflow	27
	Appendix B Experimental data	31
B.1	Vector Network Analyser results	31
B.2	Terahertz time-domain spectrometer	32

Chapter 1

Introduction

During the last decades, quantum computation has become a major research field in physics. Since Richard Feynman proposed in the 1980s the idea of using the basic principles of quantum mechanics to process information [1], many players have joined the race to reach the so-called quantum supremacy [2], which would put at stake the security of most of the cryptography systems used nowadays. These players include, for example, universities from all around the world [3], private companies such as IBM, Google or Rigetti and international initiatives like the European Quantum Flagship [4]. During these years of intense research and breakthroughs in this field, one of the main issues that these players have had to face is reducing the amount of noise in their experiments, in particular the noise caused by infrared radiation [5][6]. In this project we want to address this problem and present a possible solution based on previous research work and on measurements that we have performed.

In the present project, we begin by introducing some basics of quantum computation with its most common physical implementation [3], superconducting qubits, in order to explain the origin of the noise caused by infrared radiation. With the aim to better understand the experiments with superconducting qubits, two simulations have been performed and their results are presented in section 3. Next, we expose in section 4 the process followed to design, build and test a component that should fulfil the goal of reducing the amount of infrared radiation that can affect a superconducting qubit. Finally, the conclusions of this work are presented in section 5.

This final degree project has been conducted under the co-supervision of Dr. Pol Forn-Díaz from the Barcelona Supercomputing Centre (BSC) and Dr. Gemma Rius Suñé from the Institute of Microelectronics of Barcelona (IMB-CNM-CSIC), where the simulations shown in section 3 were carried out. Dr. Forn-Díaz belongs to the Quantic research group of the BSC which at the beginning of this project was analysing a superconducting qubit at the Catalan Institute of Nanoscience and Nanotechnology (ICN2), but on April 2019 moved to the High Energy Physics Institute (IFAE). The experiments presented in section 4 were mostly prepared and realised in these three research centres with the only exception of the measurements shown in section 4.4, which were performed at the Department of Condensed Matter Physics of the University of Barcelona (UB).

Chapter 2

Basics of quantum computation

Quantum computation uses the phenomena associated to quantum mechanics to perform quantum information processing [7]. The basic unit of a quantum processor is the qubit, which is a system described by a wavefunction that can be in a superposition of two states which are called $|0\rangle$ and $|1\rangle$ in analogy to classical computation [8]. Accordingly, an arbitrary state of a qubit can be expressed as

$$|\psi\rangle = a|0\rangle + b|1\rangle, \quad (2.1)$$

where a and b are complex numbers related to the probability of obtaining the results 0 or 1 when measuring the qubit. Another basic principle of quantum mechanics used in quantum computation is entanglement. This implies that it is possible to prepare two or more qubits in such a way that they cannot be described independently one of each other. The so-called Bell states are an example of fully entangled states [7]. For two different qubits A and B , one of these Bell states can be expressed as

$$|\psi\rangle_{AB} = \frac{1}{\sqrt{2}}(|0\rangle_A|0\rangle_B + |1\rangle_A|1\rangle_B). \quad (2.2)$$

In analogy to classical logic gates, quantum logic gates are defined as unitary operations that can be used to change the state of a system formed by one or more qubits. A sequence of quantum gates forms a quantum algorithm, which can be run in a quantum computer to tackle a certain problem [7].

The main advantage of quantum computation is that some of these quantum algorithms are capable of solving problems in shorter times than their classical counterparts. The most popular case is Shor's algorithm for factorisation of prime numbers [9]. If this algorithm was implemented in a quantum computer with a number of qubits in the order of 4,000, it would be possible to decode some of the most commonly used cryptography systems, such as RSA [10].

The DiVincenzo criteria [11] are used to determine which experimentally-validated approaches to implement qubits are better to be used in quantum processors. Here we list most of those systems [12].

1. Ion-trapped atoms [13]
2. Quantum dots [14]
3. Photons [15]
4. Topological qubits [16]
5. Superconducting qubits [17]

2.1 Superconducting qubits and Josephson Junctions

Superconducting qubits are the most widely used implementation of quantum processors [3]. They consist in a superconducting circuit which, at low temperatures, has an associated anharmonic energy spectrum. In order to better understand their working principle, one can start with a classical electric (LC) circuit, like the one shown in Figure 2.1(a).

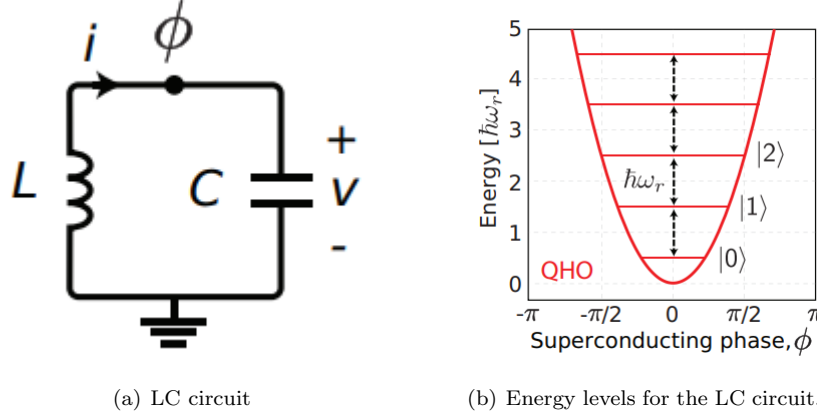


Figure 2.1: Equivalent circuit and energy levels of the LC circuit, which quantum equivalent is the QHO. The superconducting phase is related to the magnetic flux [18].

The classical Hamiltonian associated to this circuit [19] is

$$\mathcal{H} = \frac{Q^2}{2C} + \frac{\Phi^2}{2L}, \quad (2.3)$$

Where Q is the electric charge accumulated in the capacitor of capacitance C and Φ is the magnetic flux that goes through the coil of inductance L . Notice that the circuit shown in Figure 2.1(a) can also be implemented in a Coplanar Waveguide Resonator (CPW), like the one shown in Figure 2.2 [20]. The resonant frequency of this circuit is

$$w_{LC} = \frac{1}{\sqrt{LC}}. \quad (2.4)$$

We must now apply circuit quantisation [18] in order to obtain the quantum equivalent of the Hamiltonian. In order to do so, we substitute the variables Q and Φ by the mathematical operators \hat{Q} and $\hat{\Phi}$, which must obey the following commutation relation

$$[\hat{Q}, \hat{\Phi}] = i\hbar. \quad (2.5)$$

Under this transformation, the Hamiltonian of the circuit becomes

$$\hat{\mathcal{H}} = \frac{\hat{Q}^2}{2C} + \frac{\hat{\Phi}^2}{2L}. \quad (2.6)$$

Notice that this Hamiltonian corresponds to the one of the Quantum Harmonic Oscillator (QHO) [21] with frequency w_{LC} . Thus, the discrete energy levels of this system will be the ones shown in Figure 2.1(b). In

the previous section we stated that the state of a qubit is a superposition of two discrete states, so we could think that two of these energy levels could be used as a qubit. However, these states are homogeneously distributed, i.e. the separation between two of them is equal for any pair of consecutive states. Therefore, if this system interacts with a photon of frequency w_{LC} , it will not be possible to distinguish which pair of states it is coupling to. As a consequence, the quantum LC circuit is not a good system to be used as a qubit.

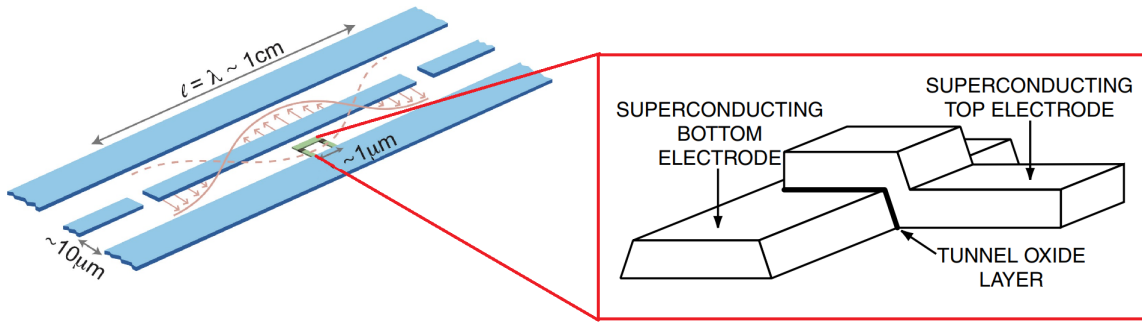


Figure 2.2: Diagram of a Josephson Junction (right) [22] placed inside a CPW resonator (left) [23]

Therefore, it is necessary to break the harmonicity, so the inductance has to be replaced by a non-linear element, such as a Josephson Junction. This consists of two superconducting materials, such as aluminium, separated by a thin layer of insulating material, aluminium oxide, acting as a tunnel junction. The schematics of a Josephson Junction placed inside a CPW resonator are shown in Figure 2.2.

The Bardeen-Cooper-Schrieffer theory for superconductivity states that, at low temperatures, bound states of two electrons (Cooper pairs) can be formed in superconducting materials [24]. All electron pairs are defined by a wavefunction which spreads over all the superconductor. Since the wavefunctions of the Cooper pairs that belong to each superconducting element is different, they have a different phase. Thus, they can be superposed and a supercurrent will appear as a consequence of the tunnel effect [21]. The inductance generated by this supercurrent has a non-linear dependence on the intensity [18]. If the inductance of our previous circuit is replaced by a Josephson Junction, as shown in Figure 2.3(a), we obtain a quantum circuit with the following Hamiltonian associated:

$$\hat{\mathcal{H}} = E_C \hat{N}^2 - E_J \cos \hat{\rho}, \quad (2.7)$$

where instead of using the total charge \hat{Q} we use the total number of Cooper pairs \hat{N} and instead of the magnetic flux we use the phase difference between the wavefunctions of the Cooper pairs that belong to each superconductor, $\hat{\rho}$. This Hamiltonian is characterised by the following parameters [25]:

- **Charging energy (E_C):** This is the energy needed to induce a charge of one electron in the junction. It is given by the expression

$$E_C = \frac{e^2}{2C}, \quad (2.8)$$

where e is the electron charge.

- **Josephson energy (E_J):** This term characterises the coupling between Cooper pairs across the junction.

The energy levels of this Hamiltonian will form an anharmonic spectrum, like the one shown in Figure 2.3(b), and we can define our qubit as the system formed by the two states with lower energy, the ground state ($|0\rangle$) and the first excited state ($|1\rangle$). Due to this anharmonicity, the separation between these two levels is unique, and the qubit will be well defined. This type of superconducting qubit is called transmon [17].

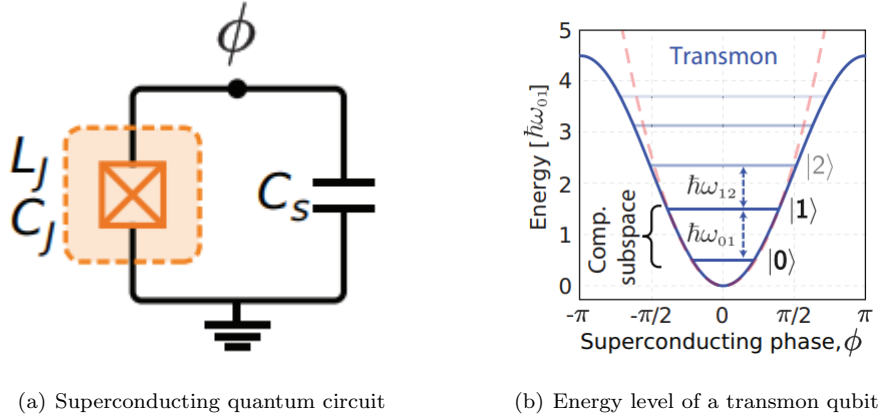


Figure 2.3: Equivalent circuit and energy levels of a transmon qubit [18].

In order to interact with these qubits, it is necessary to couple them to an electromagnetic field. One way to do this is by using stationary waves which oscillate with the characteristic frequency of the qubit. This can be achieved by placing it inside a resonator with a resonant mode equal to this frequency, since it acts as a filter that only allows electromagnetic waves of this frequency to interact with the qubit. In section 3 we will show two simulations in which the following resonating systems have been used:

- 3D Cavity resonator: The qubit is placed inside a 3-dimensional cavity made of a conducting material, such as copper. The dimensions of the cavity have to be adjusted such that a resonant mode, usually the fundamental, fits the qubit's frequency. In section 3.1 we simulate a Josephson Junction placed inside a cavity like this one.
- CPW resonator: It is also possible to use a 2-dimensional resonator such as the one shown in Figure 2.2. In order to protect them from the environment, it is common to place the CPW+qubit system inside a 3-dimensional cavity [26] with resonant modes far away from the qubit's frequency which acts as a sample box. In section 3.2 we analyse the geometry that a cavity should have in order to fulfil this condition.

2.2 Noise sources and how to reduce their impact

The state of a qubit can be a superposition of the ground and the first excited states shown in Figure 2.3(b). But the influence of the environment can cause that the excited state spontaneously decays into the ground state. This would reduce the energy of the system. The relaxation time T_1 is used to characterise the time that it takes before this happens. The relative phase between both states can also be affected by the environment. The coherence time T_2 is used to characterise the time that it takes before the state of a qubit is lost. We call noise to the effect of the environment that leads to this loss of quantum superposition. A long T_2 would allow us to implement more quantum logic gates on our qubit, and thus it would be possible to perform more complex operations [18]. A main source of this noise are the so called quasiparticles [6], which are the states that appear when one of the Cooper pairs that belong to a superconductor is broken.

The following rate equation describes the number of quasiparticles (N_{qp}) in a system at a given time [5].

$$\frac{\delta N_{qp}}{\delta t} = \frac{P}{\Delta} + G - RN_{qp}^2 \quad (2.9)$$

Let's analyse the meaning of each term of this equation. The first one stands for the generation of quasiparticles caused by the absorption of light. P represents the absorbed power while Δ is the minimum energy necessary to break a Cooper pair. In the second term we have a generation factor G that represents those quasiparticles that are generated by the thermal excitations present in our system. Finally, the last term stands for the recombination of quasiparticles, characterised by R .

In the ideal case, the influence of the absorbed power would be negligible and the density of quasiparticles would take the following form [5].

$$n_{qp} = D\sqrt{2\pi k_B T \Delta} \exp\left(\frac{-\Delta}{k_B T}\right) \quad (2.10)$$

Where D stands for the density of states and k_B is the Boltzmann constant. We can see that if this was the case, it would be enough to reduce the temperature in order to decrease the density of quasiparticles.

The qubit has to be placed in a dilution refrigerator that puts it in a thermal equilibrium at a milikelvin temperature, so we already have fulfilled the condition of low temperature. But problems arise when taking into account the term associated to the absorbed power. If this term is larger than the other ones, the density of quasiparticles will be independent of the temperature and it will be given by

$$n_{qp} \approx \sqrt{\frac{P}{\Delta}} \quad (2.11)$$

The energy gap for a typical superconductor such as aluminium is [27] $\Delta/e = 3.4 \cdot 10^{-4} \text{eV}$, which corresponds to infrared frequencies. This becomes a problem because at low temperatures there is emission of black body radiation at frequencies in this range. Consequently, it is not enough to protect the qubit from external radiation, it also has to be protected against the stray infrared photons generated inside the dilution refrigerator. In order to illustrate this better, in Figure 2.4 the Planck distribution has been represented for a temperature of 4K. We can see there that there is a big amount of black body radiation emitted above the aluminium gap.

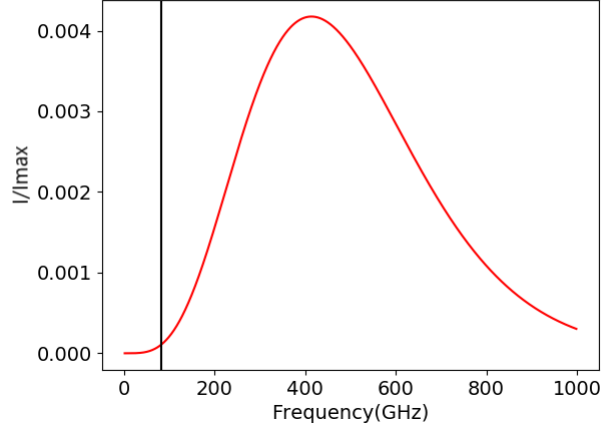


Figure 2.4: Normalised intensity of emitted black body radiation as a function of the frequency. The black vertical line indicates the frequency of the aluminium gap

It is common to use coaxial cables to send and receive the signals that interact with the qubit. One way to reduce the amount of infrared light that reaches the qubit is by placing filters in these cables that block or attenuate them [28]. In section 4 we present a way to design, build and test these filters.

Let us describe the filter as a black box with two input and output ports, like the one shown in Figure 2.5.

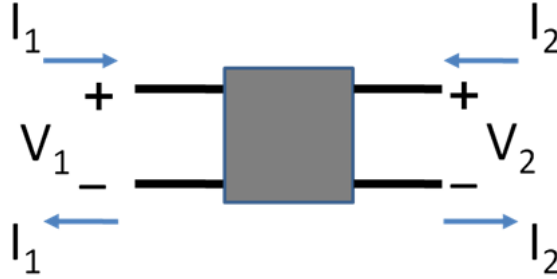


Figure 2.5: Black box representing one of the filters [29]

In order to analyse our filters, it is necessary to evaluate the S-matrix elements, which are defined as follows.

$$S_{11} = \frac{V_1^-}{V_1^+}, \quad S_{12} = \frac{V_1^-}{V_2^+}, \quad S_{21} = \frac{V_2^-}{V_1^+}, \quad S_{22} = \frac{V_2^-}{V_2^+}. \quad (2.12)$$

The magnitude of these coefficients can be expressed in logarithmic scale in units of decibels (dB). S_{12} and S_{21} will give us a measure of the relation between the intensity of the waves that are transmitted from one port to the other. Similarly, S_{11} and S_{22} will give us information on those waves that are reflected in each port [20]. Thus, we use S_{12} and S_{21} to evaluate the transmission of our filters, while S_{11} and S_{22} are used to characterise the reflection.

Chapter 3

Computational simulation

In this section we present two simulations that have been performed using the modelling software Comsol Multiphysics 5.4 [30]. This program is a finite-element solver with multiple modules that can reproduce different physical phenomena. An important feature is that it allows us to combine these modules in order to perform multiphysics analysis. For example, we can use the thermal and the electrostatics modules to study the electric voltage generated by a conductor when it is under a temperature gradient.

The main reason why this software has been chosen among other ones is that it can be used to perform very accurate studies of three-dimensional geometries, while other programs are constrained to two dimensions. The license of the software used for this project belongs to the Institute of Microelectronics of Barcelona.

As stated before, this is a finite-element solver, which means that before performing its calculations, Comsol Multiphysics must separate the analysed geometry in the different elements that form a mesh. In our simulations the mesh is formed by several tetrahedrons of different size. Since the final result must not depend on the parameters of the simulation, it is essential to perform a mesh analysis. This consists on analysing whether the outcomes of the simulation depend on the maximum size of the tetrahedrons that form the mesh.

3.1 Capacitance matrix of a Josephson Junction

As it was explained in section 2.1, the basic component of a superconducting quantum circuit is the Josephson Junction. Our goal is to determine the capacitance matrix of a circuit formed by a Josephson Junction and a capacitor using a simulation performed with Comsol Multiphysics 5.4. A description of the whole process followed can be found in Appendix A.

First, let us review the concept of capacitance matrix (\mathbf{C}). This matrix provides us with a relation between the voltages (\mathbf{V}) and the charges (\mathbf{Q}) of a set of conductors. For an arbitrary system, this would be [31]

$$\mathbf{Q} = \mathbf{C} \cdot \mathbf{V}. \quad (3.1)$$

In our analysis we have two conductors separated by an insulator, so \mathbf{C} will be a 2x2 matrix. Note that Comsol Multiphysics is not prepared to deal with superconductors at low temperatures, so for now our analysis is constrained to the case of a superconducting circuit at room temperature, i.e. in which the superconductors behave as normal conductors.

The geometry of our simulation is depicted in Figure 3.1. It consists in two components of aluminium separated by a thin layer of aluminium oxide of thickness 5nm. The superconducting circuit has been placed over a silicon substrate (Figure 3.1(b)) and all the system is enclosed by a cavity made of copper (Figure 3.1(a)), where the ground of the system has been placed. The specific sizes used for this simulation have been chosen such that our system is as similar as possible to the transmon qubit that is being analysed by the Quantic research group.

Given the voltages V_1 and V_2 that go through each conductor, the charge found on conductor 1 for our system is

$$Q_1 = (C + C_0) \cdot V_1 - C_0 \cdot V_2, \quad (3.2)$$

where C is the capacitance of the circuit's capacitor and C_0 represents the capacitive coupling of the plates to the ground. Thus, the capacitance matrix that we want to analyse takes the following form.

$$\mathbf{C} = \begin{pmatrix} C + C_0 & -C_0 \\ -C_0 & C + C_0 \end{pmatrix} \quad (3.3)$$

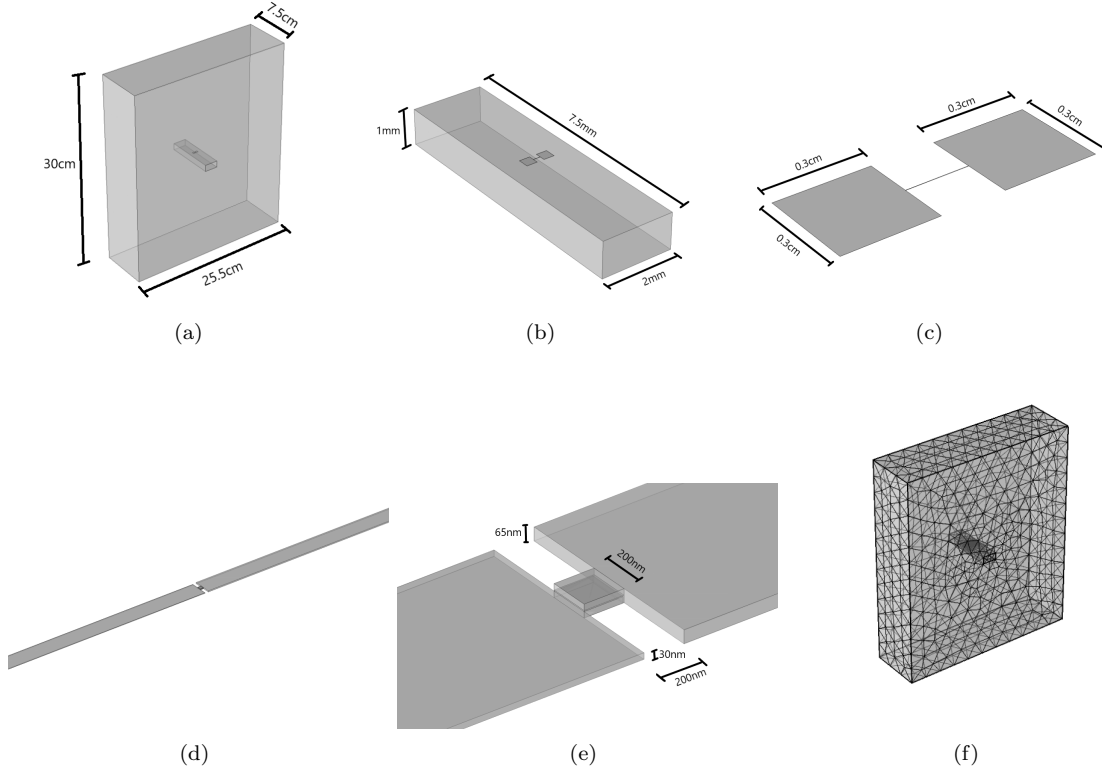


Figure 3.1: Figures (a) to (e) show the geometry of the analysed system. (f) shows the mesh used to perform the simulation.

The resulting capacitance matrix of this system is

$$\mathbf{C} = \begin{pmatrix} 74.97 & -25.97 \\ -25.97 & 74.97 \end{pmatrix} (\text{pF})$$

Using Equation (3.3) we calculate the value of our simulated capacity to be $C = 49.00\text{pF}$. Since the height of the simulated cavity is different from the height of the real cavity used by the Quantic research group, which measures 36mm we have determined the value of this capacity for different dimensions of the external cavity in order to establish whether this difference should be considered a source of error. The results can be observed in Table 3.1. The reason why it was not possible to simulate the exact dimensions of the cavity is because Comsol Multiphysics gives a geometry error. The most probable cause of this problem is that there are eight orders of magnitude of difference between the size of the Josephson Junction and of the resonant cavity, and we can expect some errors to arise from this large difference.

Dimensions	$C(\text{pF})$
4mm x 4mm x 7.5mm	53.58
5mm x 5mm x 7.5mm	51.62
6mm x 6mm x 7.5mm	50.55
10mm x 10mm x 7.5mm	49.16
25.5mm x 25.5mm x 7.5mm	49.07
25.5mm x 30mm x 7.5mm	49.00

Table 3.1: Capacitance obtained from our simulation with different values of the dimensions of the external cavity. The last row shows the result that was obtained with the initial simulation

We can see that the capacity seems to asymptotically approach a certain value every time the dimensions of the cavity are increased. Since the change in C when these dimensions approach the real sizes of the cavity are of the order of 10^{-16}F we can consider them to be negligible and conclude that there will not be any significant difference between a result obtained with our simulated cavity and one obtained with the real one. The best way to check whether this result is correct or not would be to measure the capacitance matrix of the real device that is being analysed by the Quantic research group. Since it was not possible to obtain these measurements, we have used the results found by Daniel Huber Slichter in his PhD thesis at the Siddiqi group of the University of California in Berkeley [28]. He found that the charging energy of the transmon he analysed was $E_C = 280h$ MHz. Using Equation (2.8) we find the following value for the capacitance associated to this measure:

$$C = \frac{e^2}{2E_C} = 69.1\text{pF}.$$

Taking this as a reference, the relative error of the result obtained with the simulation is of a 30%, which is pretty high but of the same order of magnitude. Considering that the geometry of the transmon analysed at the Siddiqi group is not exactly the same as the one that is being simulated we can conclude that the result obtained from the simulation is consistent with the theory.

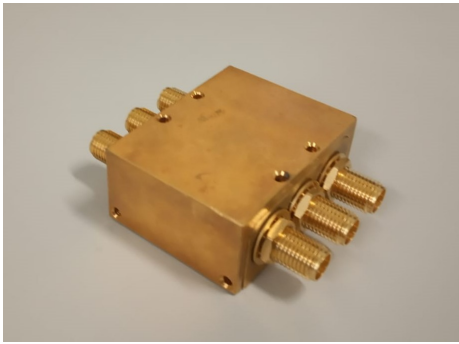
Finally, we have performed a mesh analysis with the aim of ensuring that the result obtained for the capacitance matrix does not depend on the parameters of the simulation. We have observed that the mesh does affect the outcomes of the simulation, but since the alterations are within the same order of magnitude as the capacitance this does not significantly affect our conclusions. It is likely that this dependence on the mesh is caused by the big difference between the maximum size of the tetrahedrons used to analyse the Josephson junction ($\sim 0.0025\text{mm}$) and the external cavity ($\sim 2.4\text{mm}$).

3.2 Resonant modes of a 3D cavity

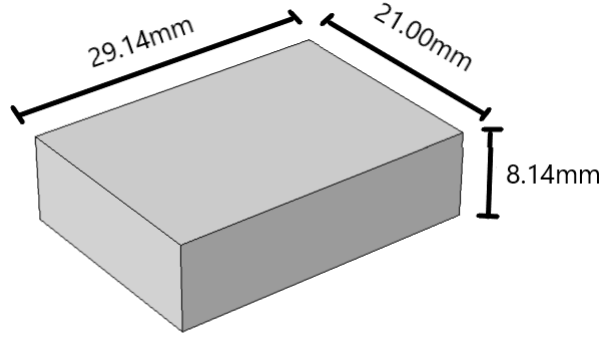
As it was explained in section 2.1, it is possible to use 2-dimensional resonators instead of resonant 3D cavities like the one used in the previous simulation. But it is still necessary to place the resonator with

the qubit inside a cavity in order to better protect them from the environment. Notice that this cavity should not act as a resonator, so its resonant modes must be as far away as possible from the characteristic frequency of the qubit.

In the Quantic research group they have a cavity prepared to be used with a CPW resonator. In this simulation, this device has been analysed in order to determine its resonant modes and check whether it is suitable to contain a CPW with a transmon qubit. In Figure 3.2(a) an image of the real cavity that we want to simulate is shown, while in Figure 3.2(b) the geometry used in the simulation with Comsol Multiphysics is depicted.



(a) Real Cavity



(b) Simulated Cavity

Figure 3.2: Cavity analysed using Comsol Multiphysics. Its structure is made of copper and its interior is considered to be empty

The radio-frequency module of Comsol Multiphysics can be used to determine the resonant modes of a cavity when we know that these will be around a certain frequency. In order to determine this reference, we can use the expression that gives the resonant frequency of the TE_{101} mode of a rectangular cavity resonator [20] filled with air.

$$f_{101} = \frac{c}{2} \sqrt{\frac{1}{a^2} + \frac{1}{b^2}} \quad (3.4)$$

Taking $a = 21.00\text{mm}$, $b = 29.14\text{mm}$ and c the speed of light in vacuum, Equation 3.4 leads to a value for this reference of $f_{101} = 8.80\text{GHz}$. Setting this as the reference frequency, the value obtained for the fundamental resonant mode of the cavity is $(8.80 \pm 0.01)\text{GHz}$. In order to check that this belongs to the first mode, and not to a higher one, the electric and magnetic fields have been plotted in Figure 3.3. Since there is only one maximum in the modulus of the electric field, we can confirm that this is the fundamental mode of the resonant cavity. It is remarkable that the result predicted by the theory is the same as the result given by the simulation, as expected considering that the simulated geometry is a perfectly rectangular cavity.

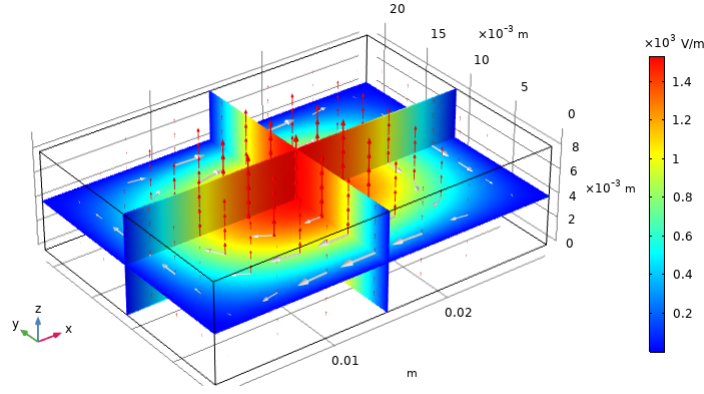


Figure 3.3: Results from the simulation. The colour plot shows the modulus of the electric field while the red and white arrows show the direction of the electric and magnetic fields respectively

The simulation has been performed using a tetrahedral mesh. In order to ensure the validity of our results, it is necessary to conduct a mesh analysis. This has been done by comparing the results obtained with different values for the maximum element size of the mesh. The outcomes are shown in Table 3.2.

Mesh Size (mm)	Res. Mode (GHz)
21.00	9.12
10.50	8.81
5.25	8.80
2.64	8.80

Table 3.2: Resonant mode obtained from the simulation as a function of the maximum element size of the mesh. The mesh used for the result shown in the last row is the same one used for Figure 3.3

From the results presented in this table we can conclude that our value, which is shown in the last row, has 3 significant figures which are not affected by the parameters of the simulation. Thus, we confirm that our simulated result for the fundamental mode of the cavity shown in Figure 3.2 is $(8.80 \pm 0.01)\text{GHz}$. The uncertainty value is obtained from the mesh analysis. Although this resonant mode is higher than the frequency of the qubit, it would be ideal if this difference was more than an order of magnitude. To achieve this goal, it would be necessary to reduce the dimensions of the cavity. Comsol Multiphysics has been used again to determine the resonant mode of an hypothetical cavity of the same thickness and height but with a width equal to 15.00mm, instead of the original 21.00mm value. As a result we obtain a resonant frequency of $(11.24 \pm 0.01)\text{GHz}$ which fulfils the condition of being higher than the usual frequency of qubits.

Chapter 4

Filtering with an epoxy coating

4.1 Previous works

As it was explained in section 2.2, it is necessary to reduce the amount of infrared light that reaches the qubit in order to increase its relaxation time T_1 . Most of this stray light is black body radiation that propagates down the lines that connect the qubit and the resonator with the outside of the dilution refrigerator. Thus, a possible approach to reduce this radiation is to place in this line a component that attenuates the amplitude of the electromagnetic waves in this range. But it is also essential that the transmission is maximum for microwaves, which are used to control the experiment.

There are some low-pass filters available in the market which sharply block the transmission at a certain frequency and they work well at low temperatures, but it has been shown [32] that they stop working properly at frequencies of the order of the THz, which can still affect the qubits. Another problem they present is that they are not impedance-matched to the transmission line, which means that those frequencies that are not transmitted will be reflected, not absorbed, and it is still possible that they reach somehow the experiment [28]. Thus, it is necessary to design a new type of filter.

A possible design was developed at Yale University [33] and it consists on placing the transmission line inside a copper box filled with an absorptive material (ECCOSORB MFS-117) which remains lossy at THz frequencies [34]. The impedance of this filter and of the transmission line is the same (50Ω), so there are no reflections and the attenuation is caused by absorption. In Figure 4.1 a comparison between the results found with this type of filter and those found with a commercial VLFX-1350 reactive filter is shown. These results were also obtained by Slichter in his PhD thesis at the Siddiqi Group [28]. We can check with these results that the commercial filter sharply cuts the transmission at a certain frequency but the attenuation diminishes with increasing frequency, reaching a peak in transmission at around 35GHz. In contrast, Slichter's filter (which he calls roach filter) does not cut the transmission so sharply, but the results measured at high frequencies remain within the noise floor of the vector network analyser used to obtain the measurements.

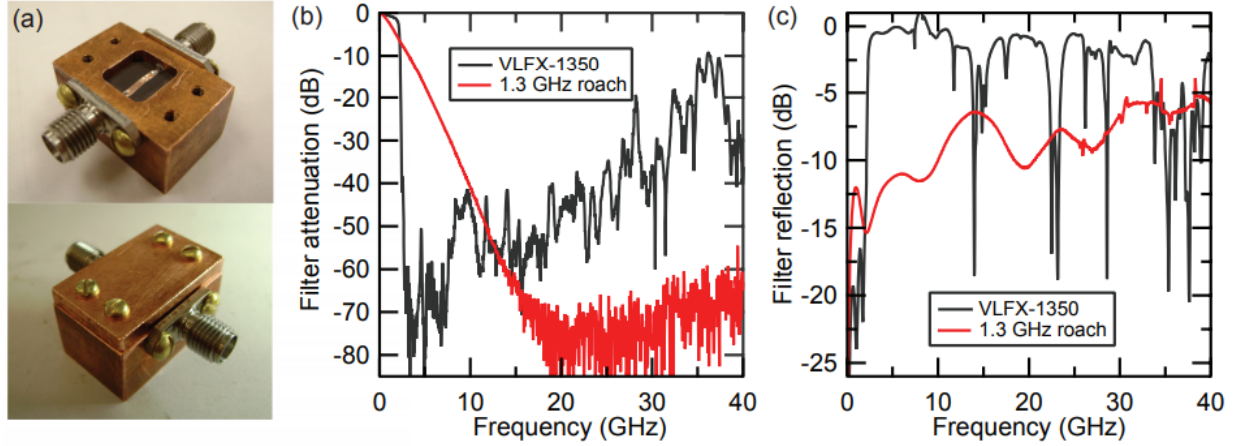


Figure 4.1: (a) shows an image of the filters used by D. H. Slichter, which have been designed to attenuate 3dB at a frequency of 1.3GHz. Notice that the line used to transmit the signal is a microstrip line. (b) shows the comparison of the results obtained for the attenuation with these filters (red) and with a commercial VLFX-1350 reactive filter (black), while (c) compares the reflection of both filters.

4.2 Design and fabrication process

The filter designed for this project is based on the one designed by Slichter, which gives the results shown in Figure 4.1. The software Autodesk Inventor 2019 has been used to design the copper box that forms the body of the filter. The sketch of this piece is shown in Figure 4.2, together with the real piece after the design was implemented at the mechanical workshop of ICN2.

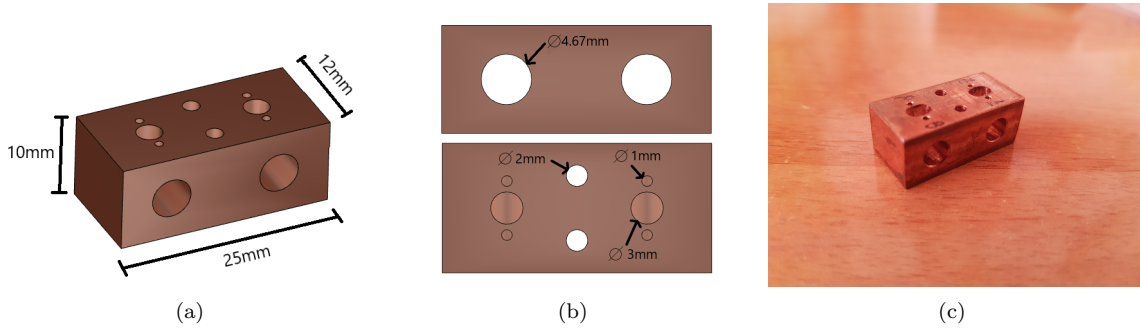


Figure 4.2: (a) and (b) show the design of the copper piece developed using Autodesk Inventor 2019. The holes shown in the upper image of (b) are of the same diameter as a SMA connector, and they were made with a more precise tool. (c) shows the copper piece after being produced at ICN2's mechanical workshop.

In usual qubit experiments, signals are transported through coaxial cables. In order to connect to our filter box we use two Amphenol SMA connectors. These contain one pin each which has been soldered to a piece of copper cable, as shown in Figure 4.3(a). To assemble the filters, two different methods have been followed. For the first one we have used Loctite Super-Glue to ensure that the SMA connectors are fixed to the body of the filter. For the second one, a thin layer of solder metal is placed in the part of the SMA that goes inside the copper piece to ensure the connectivity between both components. Then the filter is

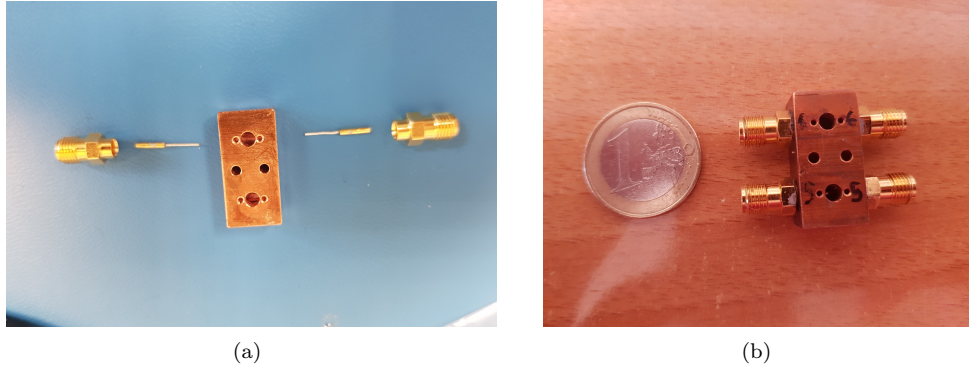


Figure 4.3: Images of the filters before and after assembling it

assembled using heat to melt this thin layer. The assembled filter is shown in Figure 4.3(b). Then comes the most delicate part of the process, since the two copper cables have to be soldered through the 3mm hole. Due to the complexity of this final step, it was performed by a technician of the electronics workshop at IFAE.

A total of eight filters have been assembled (two per copper box). In order to ensure that they are correctly built, it is necessary to characterise them by obtaining their S-matrix elements.

The final step would be to introduce the absorptive material through the 3mm hole, while the air leaves the filter through the two 1mm holes. Since it was not possible to complete this stage, an analysis of different samples of absorptive material has been performed instead. The results are shown in section 4.4.

4.3 Filter characterisation

As explained in section 2.2, the S-matrix elements can be used to evaluate the transmission and reflection of our filters as a function of the frequency. This allows us to establish whether they are well built or not, since a bad connectivity between the SMA connector and the copper piece would lead to a resonance in these parameters. In Figure 4.4 a comparison is depicted between two filters that were built following the two methods previously exposed. The measurements were taken with a Vector Network Analyser (VNA) Agilent Technologies E5071B, property of IFAE.

In Figure 4.4(a) it is possible to observe a resonance at a frequency of 30MHz, since for this value the transmission decreases abruptly to -27dB while the reflection becomes maximum. This means that signals of this frequency do not reach the filter, they are reflected by the connection between the SMA and the copper piece. We can also observe a sharp decrease of reflection at 340MHz.

This evidences that there is not a good connectivity between the filter body and the SMA when the first method described in section 4.2 is used. For this reason it is necessary to dismantle it and assemble it again using the second method, which from Figure 4.4(b) it can be deduced that is better. We see that with this method the transmission has a constant and maximum value. This is what we wanted, since the analysed frequencies belong to the microwave regime. As it was explained before, these frequencies must be maximally transmitted, since they are the ones used to control the qubit. We have performed the same analysis with all the filters and the second building method always gave the best results. Thus, we have dismantled all the filters that had been built using the first method and we have assembled them again using the second method. In Appendix B.1 the results of the characterisation of 5 of our filters are shown, and all of them show a behaviour similar to the one depicted in Figure 4.4(b).

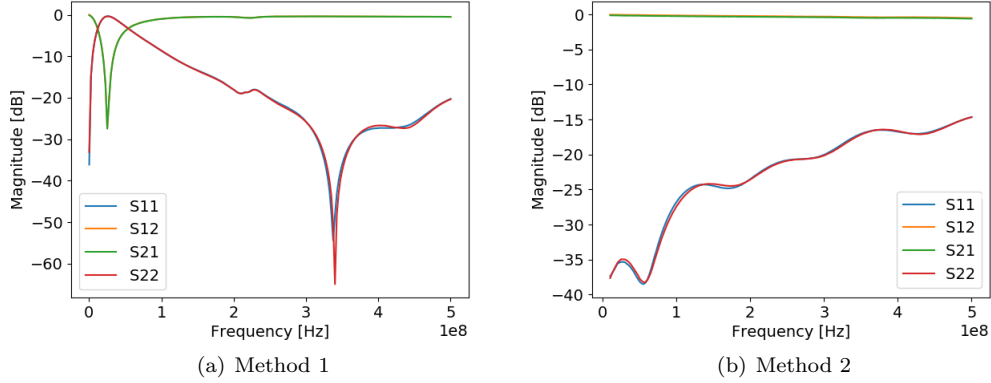


Figure 4.4: Transmission and reflection parameters for two filters built using the two methods exposed in section 4.2. The lines representing S12 (yellow) and S21 (green) are superposed, and the same happens for S11 (blue) and S22 (red).

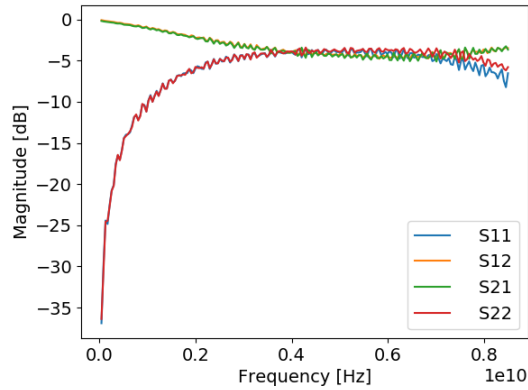


Figure 4.5: S-matrix elements of the filter built with the second method for all the frequency range that can be analysed with the VNA

In Figure 4.5 we show the S-matrix elements for the same filter as in Figure 4.4(b) but in the frequency range between 300kHz and 8.5GHz. From these results we can deduce that the filters are not impedance-matched to the coaxial cables, since the reflection coefficients take very high values [20]. As shown in Figure 4.1, when the filter is filled with the absorptive material the reflection should decrease.

4.4 Epoxy absorption analysis

As it was explained in section 4.2, the filter must be filled with an absorptive material that causes the attenuation of infrared radiation. We have used the Stycast 2850FT epoxy, a material similar to the Eccosorb epoxy [34] that Slichter used in his thesis. We have mixed Stycast with silicon carbide (SiC) grains, since in the work done by *Klaassen et al.* [35] it was shown that photons bounce off SiC grains of the same size as their wavelength. This increases the probability of being absorbed by Stycast. Here we wanted to deepen into this phenomenon and for this reason we have produced a total of 18 samples of

different thickness in which we used different concentrations of SiC grains of size $100\mu\text{m}$ and 1mm . A 19th sample with just Stycast was also produced. In Table 4.1 the characteristics of each sample are specified.

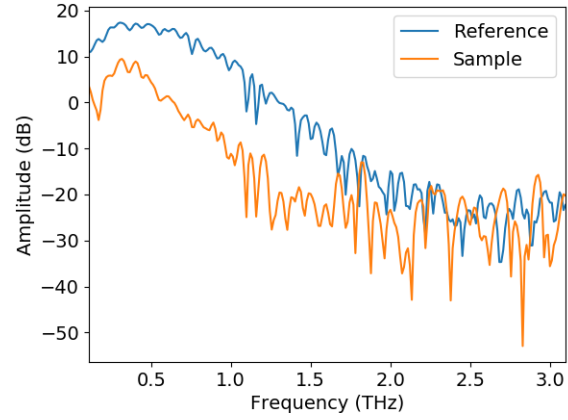
Sample	SiC $100\mu\text{m}$	SiC 1mm	Thickness
1	1:8	-	2mm
2	1:8	-	1mm
3	1:8	-	0.5mm
4	-	1:8	2mm
5	-	1:8	1mm
6	-	1:8	0.5mm
7	1:16	1:16	2mm
8	1:16	1:16	1mm
9	1:16	1:16	0.5mm
10	1:4	-	2mm
11	1:4	-	1mm
12	1:4	-	0.5mm
13	-	1:4	2mm
14	-	1:4	1mm
15	-	1:4	0.5mm
16	1:8	1:8	2mm
17	1:8	1:8	1mm
18	1:8	1:8	0.5mm
19	-	-	1.65mm

Table 4.1: Characteristics of the different samples analysed. The second and third columns show the ratio between the mass of Stycast and of SiC that each sample contains. The thicknesses in the third column are the thicknesses of the mould used to produce the samples, except the last one which was determined using a calliper.

In order to determine the transmission of these samples we have used a Zomega Terahertz Mini-ZTM time-domain spectrometer, property of the Condensed Matter Physics Department of the University of Barcelona. With this instrument we can analyse the amplitude of the waves transmitted for frequencies between 100GHz and 12.5THz . In Figure 4.6 an image of one of the samples is shown, together with the measurements obtained with this instrument. From these results we can deduce that the noise floor of this instrument is below the -20dB of amplitude. The results obtained for the remaining 18 samples follow a shape similar to the one shown in Figure 4.6. They are presented in Appendix B.2.



(a) Photography of Sample 1

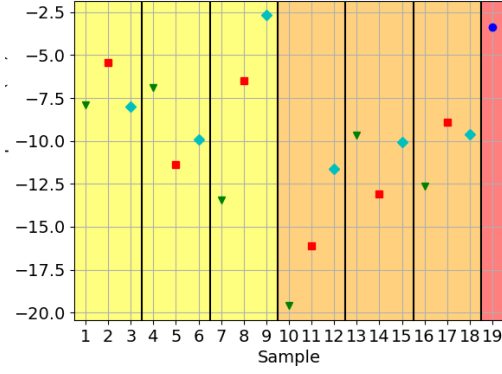


(b) Transmitted amplitude for Sample 1

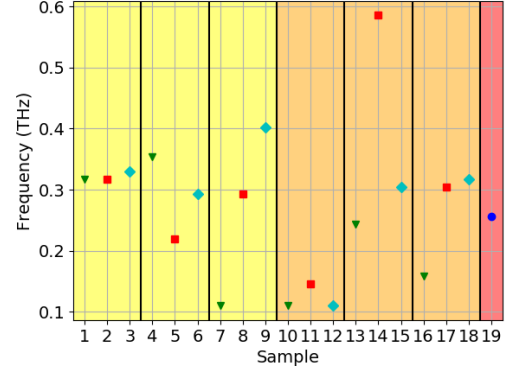
Figure 4.6: Analysis of the transmitted amplitude of Sample 1, compared with the transmitted amplitude obtained when no sample is placed in the time-domain spectrometer (Reference).

The optimal sample should fulfil the following requirements in the range of frequencies analysed:

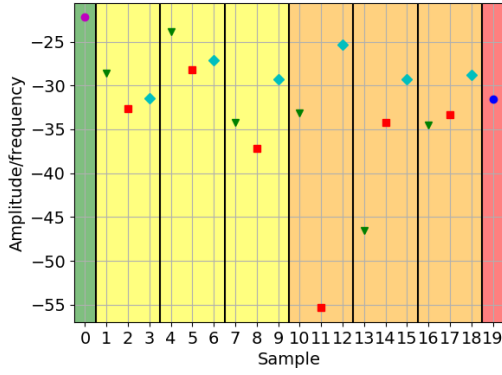
1. The maximum amplitude transmitted should be as small as possible. In Figure 4.7(a) this value is represented for each sample.
2. This maximum should be found at the lowest frequency possible. The frequency associated to the maximum transmitted amplitude for each sample is shown in Figure 4.7(b)
3. The decrease in the transmitted amplitude should be abrupt. This can be analysed using a linear regression between the point of maximum transmitted amplitude and the last point before reaching the noise floor of -20dB. The slope of this regression for each sample is shown in Figure 4.7(c), while the r^2 coefficient is presented in Figure 4.7(d). Since there is no reason to believe that the amplitude will decrease linearly, we have also calculated the total area below the curve formed by the transmitted amplitude and it is shown in Figure 4.7(e).



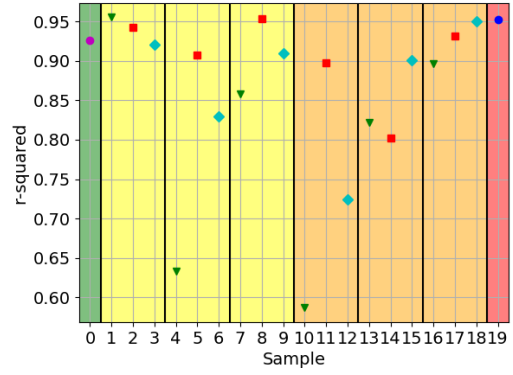
(a) Maximum amplitude measured for each sample.



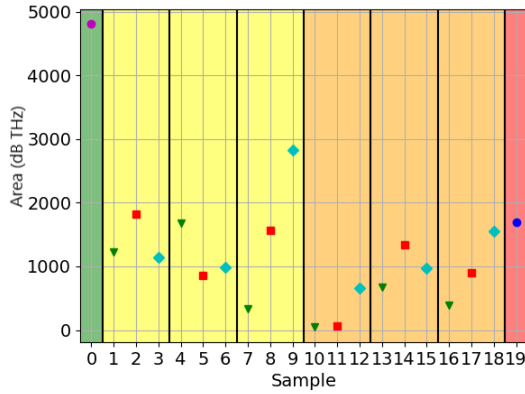
(b) Frequency of the maximum amplitude.



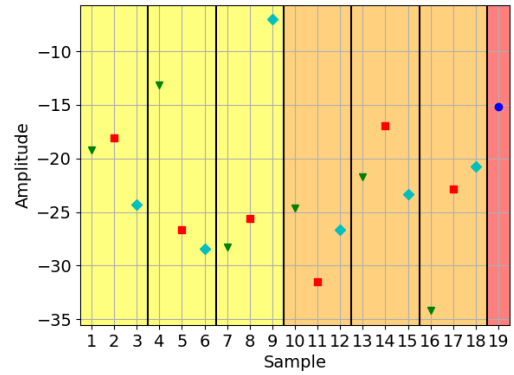
(c) Slope of the linear regression.



(d) r^2 coefficient of the regression.



(e) Area under the curve formed by the transmitted amplitude.



(f) Amplitude transmitted at 1THz.

Figure 4.7: Results obtained from the data shown in Appendix B.2. The numbers in the x-axis represent the same as the numbers in the sample column of Table 4.1, with the exception of 0, which represents the reference in those graphics in which it has not been subtracted. The points with the same shape and colour represent samples of the same width. The black vertical lines separate the groups of samples with SiC of different sizes. The background colour characterises the samples with the same concentration of SiC.

In order to establish which are the best and worst samples we have analysed the results shown in Figure 4.7 and we have detected those values that stand out among the other ones. In Table 4.2 we expose those samples that we consider better and worse than the other ones for each graphic and we explain the criterion followed to discriminate them.

Graphic	Best samples	worst samples	Further remarks
Amplitude Maximum (Figure 4.7(a))	7, 10, 11, 14, 16	2, 4, 9, 19	The best samples present an amplitude below -12.5dB while the worst ones presents an amplitude above -7.5dB
Frequency of the amplitude maximum (Figure 4.7(b))	7, 10, 11, 12, 16	9, 14	The frequency of the maximum amplitude for the best samples is below 0.2THz and for the worst samples is above 0.4THz
Slope of the linear regression (Figure 4.7(c))	8, 11, 13	4, 6, 12	The slope of the regression for the best samples is below -35dB/THz and for the worst samples it is above -27db/THz
r^2 coefficient of the linear regression (Figure 4.7(d))	-	4, 6, 10, 12, 13, 14	The worst samples are those with r^2 lower than 0.85. It is not possible to determine which are the best ones due to the similarity of r^2 for the remaining samples.
Area below the amplitude curve (Figure 4.7(e))	7, 10, 11, 16	Reference, 9	The best samples present an area smaller than 500 dB·Hz. The worst results have been found with the reference and with sample 9, which present areas above 2000 dB·Hz.

Table 4.2: Analysis of the values represented in the graphics shown in Figure 4.7

It is also insightful to use the values for the amplitude obtained at a reference frequency, such as 1THz (Figure 4.7(f)), in order to determine the transmitted amplitude per unit of thickness for each type of sample. This can be achieved by calculating the slope of a linear regression between the three points of different thicknesses that contain the same concentration of SiC. These results are shown in Table 4.3. We can see that they present a low correlation coefficient, so in general they are not reliable to extract any conclusion. Using the same criterion as in Table 4.2 for the data from Figure 4.7(d), the only conclusion we can extract from these results is that the mix of Stycast with both types of SiC grains at a concentration 1:4 attenuates 9.32dB/mm. We have discarded the result obtained for the mixture of Stycast with SiC grains of 1mm at 1:8 because during the production process of sample 4 small holes appeared where signal might have leaked.

The bad results shown in Table 4.3 can be caused by some problems that arose during the production process of the samples. Initially, the Stycast epoxy is a fluid that has to be mixed with a catalyst that initialises its solidification. In this case, the Stycast started to solidify before we had placed it in the moulds, making it more difficult to manipulate. For this reason, it was not possible to produce samples of the exact same thickness as the moulds. Thus, the thickness associated to each sample in Table 4.1 might not be very accurate.

In Table 4.2 we can see that sample 11 always fulfils the criteria to be considered a good result. This

Material	1:8		1:4	
	Slope (dB/mm)	r^2	Slope (dB/mm)	r^2
Stycast + SiC 100 μ m	2.73	0.403	2.11	0.210
Stycast + SiC 1mm	10.64	0.949	0.254	0.003
Stycast + SiC 100 μ m + SiC 1mm	-12.53	0.684	-9.32	0.964

Table 4.3: Amplitude per unit of space at 1THz for the different analysed concentrations of SiC.

corresponds to a sample of width 1mm in which Stycast is mixed with 100 μ m SiC in a mass proportion 1:4, as it is explained in Table 4.1. In the same table we see that samples 7 and 16 contain the same types of SiC at different concentrations. These two samples present a similar behaviour and they are considered good samples in all the analysis except for the linear regression. As it was stated before, the linear regression and the area under the curve are used to study how sharp is the amplitude decrease between the maximum and the noise floor of the measuring instrument. Thus, the fact that the analysis of the area leads to a satisfying result for a certain sample but the linear regression does not, might mean that this decrease is not linear. Since this is not relevant at all for our analysis, we can conclude that samples 7 and 16 also give good results. Another outcome worth remarking is sample 10, which shows a similar behaviour to that of samples 7 and 16, although its composition is exactly equal to sample 11. So we can conclude that the best mixtures to use in our filters are either Stycast with both types of SiC or Stycast with 100 μ m SiC.

The sample that gives the worst results following the criteria stated in Table 4.2 is number 9. This sample has a width of 0.5mm and contains a mix of Stycast with both types of SiC at a mass concentration 1:16:16. Sample 4 also gives bad results, especially with the linear regression, but as it was explained before this sample should be discarded due to the problems that occurred during its production.

It is also interesting to perform a separate analysis of the data shown in Figure 4.7 for sample 19, which is composed only by Stycast. We can conclude that most of the results obtained with a mix between Stycast and SiC give better results than this sample, which means that it is a good idea to include SiC in the absorptive material used to build the filters, as it was already shown by *Klaassen et al.* [35].

Those samples that have not been mentioned (1, 2, 3, 5, 6, 8, 12, 13, 14, 15, 17 and 18) gave very similar results and it is not possible to use the analysed data to determine which are better than the other ones.

From this analysis we have deduced that samples 7, 10, 11 and 16 give the best results, so the best mixtures to use in our filters are either Stycast with both types of SiC or Stycast with 100 μ m SiC. It is worth noting that the measurements taken in this section should be repeated in order to ensure that the results obtained have not been affected by the production process. To determine which of the two mixtures is the best one, it would be interesting to create more samples with more varied concentrations and analyse them.

It is remarkable that in the literature we have found several analysis on the effects of mixing Stycast with SiC grains of many sizes [5] [35], but we have not found any study on the effects of mixing more than one size of SiC grains. If it was possible to show that the mixture of Stycast with SiC of 1mm and of 100 μ m presents a better absorption than the other ones, this information would be very valuable for those research groups that work on experimental quantum computing with superconducting qubits.

Chapter 5

Conclusions

The main goal of this project has been to find a way to improve the coherence time of a superconducting qubit. In order to achieve this goal, we performed two simulations which are shown in section 3. The first one showed that the capacitance matrix of a Josephson Junction simulated using Comsol Multiphysics gives a result of the same order of magnitude as the one measured in the literature.

The second simulation has been performed with the same software and we have used it to determine the resonant modes of one of the cavities used by the Quantic research group. The results show that the first mode is at a frequency of $(8.80 \pm 0.01)\text{GHz}$, which is not ideal since we want it to be much higher than the characteristic frequency of the qubit. Using Comsol Multiphysics we have concluded that if one of the sides of the cavity was reduced from 21.00mm to 15.00mm a resonant mode of $(11.24 \pm 0.01)\text{GHz}$ would be obtained, which fulfils the required condition.

In section 4 we have presented a component that can be used to attenuate infrared radiation, which we call infrared filter. We have explained the process that has been followed to design and build it. We have shown that the characterisation of the filter can be used to determine whether it is well built or not, as in Figure 4.4.

We have finally analysed different mixtures of Stycast 2850FT with SiC grains of different sizes in order to determine which shows the minimum transmitted amplitude. The results are summarised in Table 4.2 and we can conclude that the best candidates to use in our experiment are the mixture of Stycast with both types of SiC (1mm and $100\mu\text{m}$) and the mixture of Stycast with SiC of $100\mu\text{m}$.

In order to obtain a more precise conclusion the measurements must be repeated and different concentrations of these two cases have to be analysed. Once one of the mixtures has been chosen, it has to be used to fill the filters and characterise them again with the aim of establishing their S-matrix elements and compare them with results found in the literature. The final test would be measuring the coherence time of a superconducting qubit placed inside a dilution refrigerator before and after installing the filters. This is left as future work.

Acknowledgements

I would like to thank Dr. Pol Forn-Díaz and Dr. Gemma Rius for giving me the opportunity of conducting my degree project in such an amazing field. The guidance and support they have granted me has been essential to carry out this dissertation. I also want to acknowledge BSC, IMB-CNM, IFAE and the Department of Condensed Matter Physics of the UB for allowing me to work in their facilities. I am especially grateful to the technicians of IFAE for the tips and help that they offered me while performing the most technical parts of this project. I would also like to thank the Quantic research group for their warm welcome and for allowing me to take part in their group meetings and events. They have shown me what an actual research group looks like. Finally, it would have been impossible to conduct this project without the patience and support of my parents and friends, who have been by my side during the good and the bad moments of the last months. *Voy!*

Bibliography

- [1] David Deutsch and Artur Ekert. “Quantum computation”. In: *Physics World* 11.3 (1998), p. 47.
- [2] John Preskill. “Quantum computing and the entanglement frontier”. In: *arXiv preprint arXiv:1203.5813* (2012).
- [3] Doug Finke. *Quantum Computing Report*. URL: <https://quantumcomputingreport.com/players/> (visited on 05/20/2019).
- [4] *European Quantum Flagship*. URL: <https://qt.eu/> (visited on 06/01/2019).
- [5] Rami Barends et al. “Minimizing quasiparticle generation from stray infrared light in superconducting quantum circuits”. In: *Applied Physics Letters* 99.11 (2011), p. 113507.
- [6] Antonio D Córcoles et al. “Protecting superconducting qubits from radiation”. In: *Applied Physics Letters* 99.18 (2011), p. 181906.
- [7] Michael A Nielsen and Isaac L Chuang. “Quantum information and quantum computation”. In: *Cambridge: Cambridge University Press* 2.8 (2000), p. 23.
- [8] John Preskill. “Lecture notes for physics 229: Quantum information and computation”. In: *California Institute of Technology* 16 (1998).
- [9] Peter W Shor. “Polynomial-time algorithms for prime factorization and discrete logarithms on a quantum computer”. In: *SIAM review* 41.2 (1999), pp. 303–332.
- [10] Tim Moses. *Quantum Computing and Cryptography. Their impact on cryptographic practice*. URL: https://www.entrust.com/wp-content/uploads/2013/05/WP_QuantumCrypto_Jan09.pdf (visited on 06/01/2019).
- [11] David P. DiVincenzo. “The Physical Implementation of Quantum Computation”. In: *Fortschritte der Physik* 48.9-11 (2000), pp. 771–783. DOI: 10.1002/1521-3978(200009)48:9/11<771::AID-PROP771>3.0.CO;2-E.
- [12] Andrew Daley. *Physical implementations of quantum computing*. URL: http://quantum.phys.cmu.edu/QCQI/QC_CMU1 (visited on 05/11/2019).
- [13] J. I. Cirac and P. Zoller. “Quantum Computations with Cold Trapped Ions”. In: *Phys. Rev. Lett.* 74 (20 May 1995), pp. 4091–4094. DOI: 10.1103/PhysRevLett.74.4091. URL: <https://link.aps.org/doi/10.1103/PhysRevLett.74.4091>.
- [14] Daniel Loss and David P. DiVincenzo. “Quantum computation with quantum dots”. In: *Phys. Rev. A* 57 (1 Jan. 1998), pp. 120–126. DOI: 10.1103/PhysRevA.57.120. URL: <https://link.aps.org/doi/10.1103/PhysRevA.57.120>.
- [15] Pieter Kok et al. “Linear optical quantum computing with photonic qubits”. In: *Rev. Mod. Phys.* 79 (1 Jan. 2007), pp. 135–174. DOI: 10.1103/RevModPhys.79.135. URL: <https://link.aps.org/doi/10.1103/RevModPhys.79.135>.
- [16] A. Y. Kitaev. “Fault-tolerant quantum computation by anyons”. In: *Annals of Physics* 303 (Jan. 2003), pp. 2–30. DOI: 10.1016/S0003-4916(02)00018-0. eprint: [quant-ph/9707021](https://arxiv.org/abs/quant-ph/9707021).
- [17] Jens Koch et al. “Charge-insensitive qubit design derived from the Cooper pair box”. In: *Physical Review A* 76.4 (2007), p. 042319.
- [18] Philip Krantz et al. “A Quantum Engineer’s Guide to Superconducting Qubits”. In: *arXiv preprint arXiv:1904.06560* (2019).

- [19] Paul A Tipler and Gene Mosca. *Physics for scientists and engineers*. Macmillan, 2007.
- [20] D.M. Pozar. *Microwave Engineering*. Wiley, 2004. ISBN: 9780471448785. URL: <https://books.google.es/books?id=4wzpQwAACAAJ>.
- [21] David J Griffiths and Darrell F Schroeter. *Introduction to quantum mechanics*. Cambridge University Press, 2018.
- [22] Michel H Devoret and John M Martinis. “Implementing qubits with superconducting integrated circuits”. In: *Experimental aspects of quantum computing*. Springer, 2005, pp. 163–203.
- [23] Alexandre Blais et al. “Cavity quantum electrodynamics for superconducting electrical circuits: An architecture for quantum computation”. In: *Physical Review A* 69.6 (2004), p. 062320.
- [24] Terry P Orlando and Kevin A Delin. *Foundations of applied superconductivity*. Vol. 8. Addison-Wesley Reading, MA, 1991.
- [25] Peter Ågren. “Charging effects in small capacitance Josephson junction circuits”. PhD thesis. Fysik, 2002.
- [26] M Göppl et al. “Coplanar waveguide resonators for circuit quantum electrodynamics”. In: *Journal of Applied Physics* 104.11 (2008), p. 113904.
- [27] Charles Kittel. *Introduction to solid state physics*. Vol. 8. Wiley New York, 1976.
- [28] Daniel Huber Slichter. PhD Thesis. *Quantum jumps and measurement backaction in a superconducting qubit*. University of California, Berkeley, 2011.
- [29] *Two-Port Network*. URL: https://en.wikipedia.org/wiki/Two-port_network (visited on 05/04/2019).
- [30] *Comsol Multiphysics*. URL: <https://www.comsol.com/> (visited on 06/09/2019).
- [31] E Di Lorenzo. “FastFieldSolvers”. In: *The Maxwell Capacitance Matrix, White Paper* (2011).
- [32] K Bladh et al. “Comparison of cryogenic filters for use in single electronics experiments”. In: *Review of scientific instruments* 74.3 (2003), pp. 1323–1327.
- [33] DF Santavicca and DE Prober. “Impedance-matched low-pass stripline filters”. In: *Measurement Science and Technology* 19.8 (2008), p. 087001.
- [34] Mark Halpern et al. “Far infrared transmission of dielectrics at cryogenic and room temperatures: glass, Fluorogold, Eccosorb, Stycast, and various plastics”. In: *Applied Optics* 25.4 (1986), pp. 565–570.
- [35] TO Klaassen et al. “Absorbing coatings and diffuse reflectors for the Herschel platform sub-millimeter spectrometers HIFI and PACS”. In: *Proceedings, IEEE Tenth International Conference on Terahertz Electronics*. IEEE. 2002, pp. 32–35.

Appendix A: Simulation workflow

In this appendix, the process followed to build the simulation presented in section 3.1 is shown. The software used is Comsol Multiphysics 5.4. The first step after executing the program is choosing the space dimensions of our system. Here we choose a 3D space. We are now given the option to select which modules to use in the simulation. For our case we choose the Electrostatics module, which is found under the tab AC/DC. In the last choice we select which type of study we want to perform. Since we are interested in a system in equilibrium which does not evolve in time, we choose the stationary study. Comsol's display should be as depicted in Figure 1.

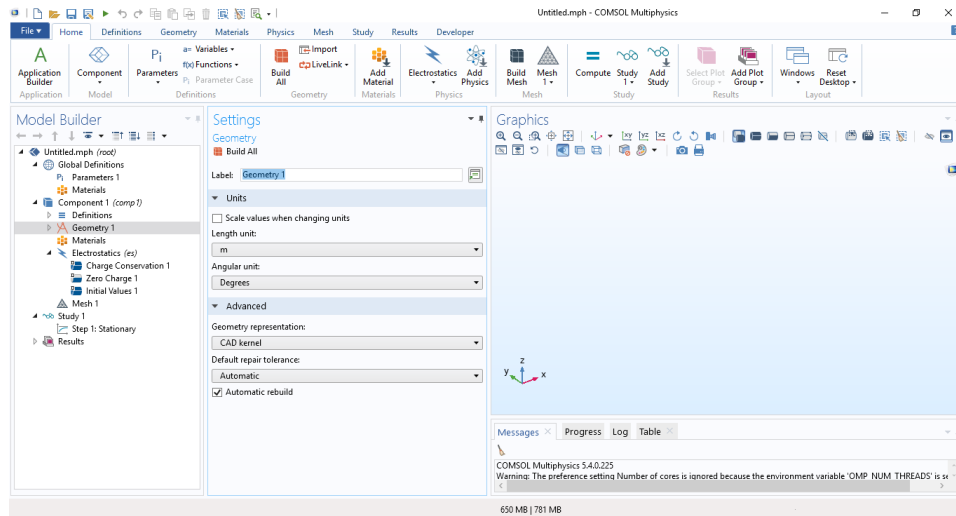


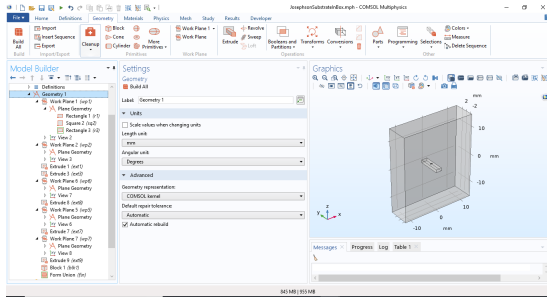
Figure 1: Initial display of Comsol Multiphysics after choosing a 3D space

We now go to the "Parameters" tab that appears in the left-hand side menu and define the parameters that our simulation will have, which are shown in Figure 2. The need of the PortName parameter will be explained later.

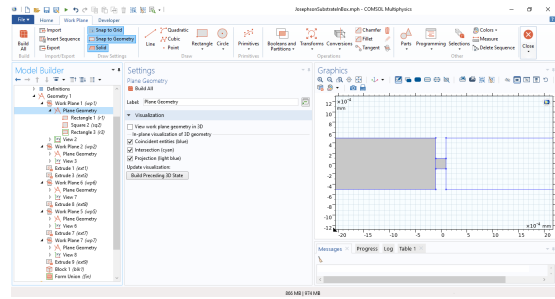
Name	Expression	Value	Description
a	200[nm]	2E-7 m	Side square junction
b	1[um]	1E-6 m	width wire junction-plates
c	300[um]	3E-4 m	Side square plates
d	100[um]	1E-4 m	length wire junction-plates
e	5[nm]	5E-9 m	height insulator junction
f	30[nm]	3E-8 m	height conductor junction
g	7.5[mm]	0.0075 m	width substrate
k	1[mm]	0.001 m	height substrate
l	2[mm]	0.002 m	length substrate
m	25.5[mm]	0.0255 m	width cavity
n	g	0.0075 m	height cavity
o	30[mm]	0.03 m	length cavity
PortName	nan	NaN	

Figure 2: Parameters used in the simulation

With these parameters we can start building our geometry using the options displayed in the "Geometry" tab. The final geometry of our simulation is depicted in Figure 3(a). Note that we have used work-planes to design the internal structures of our system, such as the Josephson Junction. An example can be observed in Figure 3(b).



(a) Full geometry of our system



(b) Example of work-plane

Figure 3: Screenshots of the geometry used.

The next step is assigning a material to each component of our geometry. In this case we have assigned Aluminium to each plate of the capacitor and Aluminium Oxide to the thin layer that separates them. The substrate is made of Silicon and the external cavity is filled with air and with Copper in its boundaries.

We must now establish the parameters of the Electrostatics module. Clicking on "Electrostatics" in the left-bar menu we go to the Manual Terminal Sweep Settings tab to activate the manual terminal sweep. Here is where we use the parameter PortName as the sweep parameter name. We now right-click on "Electrostatics" and we add a ground and two terminals. With the ground we can set the zero-voltage element on the surface of the copper cavity. The two terminals are placed in each of the plates of the capacitor and they are given an initial voltage of 1V, although this is irrelevant when calculating the capacitance matrix. Notice that each terminal has assigned a name, 1 or 2. This means that depending on the value of PortName, the analysis will be performed with either terminal 1 or 2. The configuration of Terminal 1 is depicted in Figure 4.

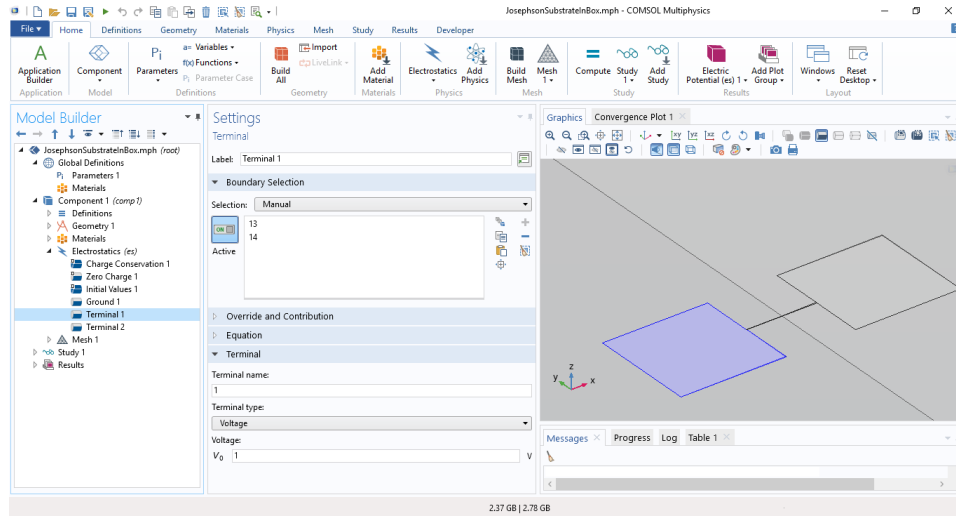


Figure 4: Configuration of the Electrostatics module

In the following step the mesh has to be configured. Since there is a big difference between the size of the cavity and the size of the Josephson Junction, it is necessary to use custom mesh, instead of a predefined one. Under the "Mesh" tab we can modify the element size of the default mesh that will be used in our system. Here we use a predefined fine mesh, which should be enough to obtain accurate results for the cavity and the substrate. We now right-click on Mesh and add a Free Tetrahedral and its own Size setting. In the Geometric Entity Selection of this setting we select all the domains that form the capacitor and the Junction. Changing the Element Size to custom we can edit the Element Size Parameters and use the ones shown in Figure 5. When performing the mesh analysis, we will use different values for the Maximum element size. Notice that several Warnings appear under the Free Tetrahedral 2 tab, which are caused by the big difference between both meshes used.

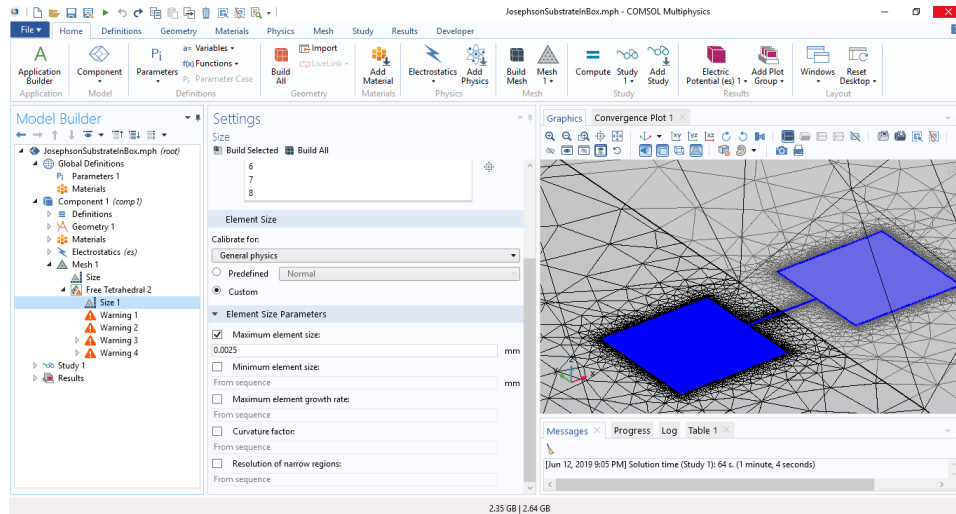


Figure 5: Screenshot of the mesh used for the capacitor and the Josephson Junction

The final step is setting the study. To compute the capacitance matrix we need the results from both

terminals that we included in Electrostatics. For this reason it is necessary to add a Parametric Sweep over the PortName parameter with the values 1 and 2, as shown in Figure 6. At this point we can run the simulation by clicking the "Compute" button.

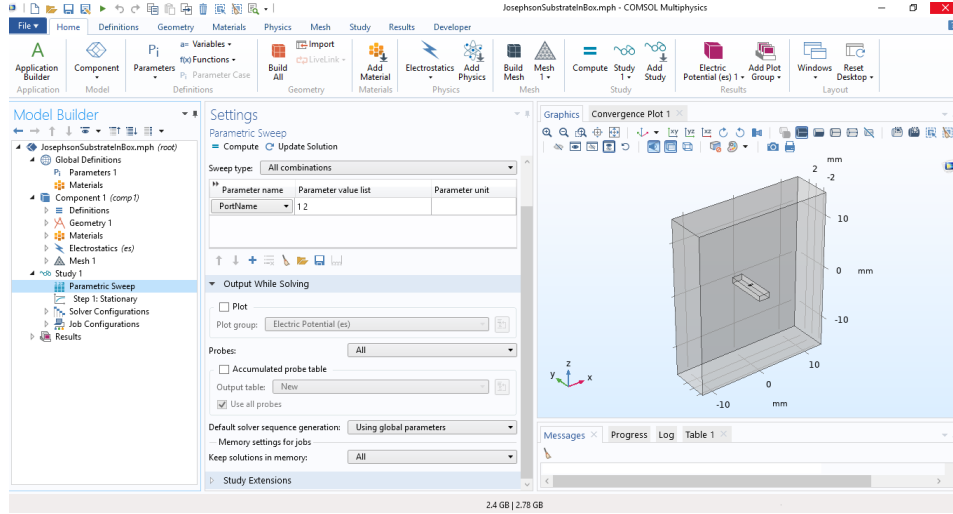


Figure 6: Screenshot of the study used for the simulation

The first result that we see is a Multislice 3D plot of the Electric Potential. To obtain the capacitance matrix we right-click on Derived Values, under the Results tab, and we add a Global Matrix Evaluation. We choose the Parametric Solutions as the Data set and we select the Maxwell Capacitance in the menu that appears when clicking the two triangles on the right side of the Expression tab. When clicking Evaluate, a table will appear with the capacitance matrix, as it is depicted in Figure 7.

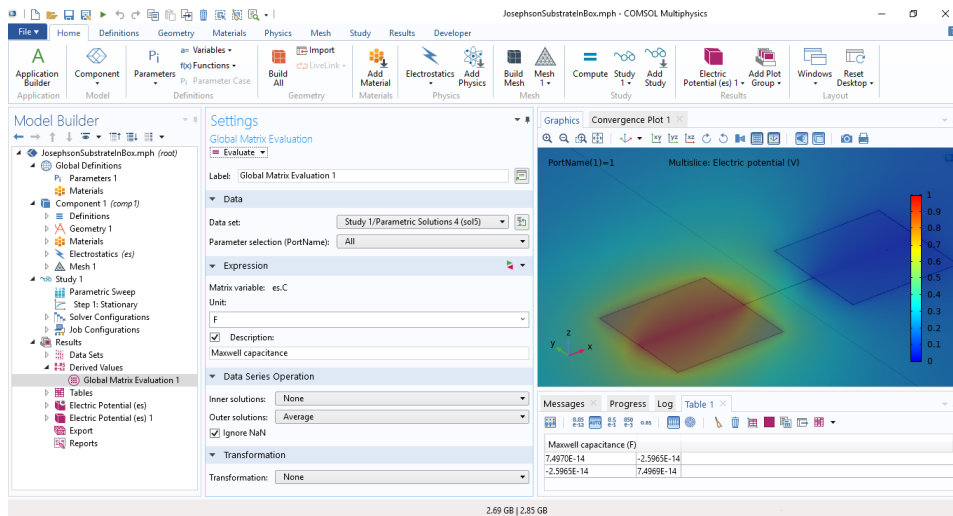


Figure 7: Final result of the simulation for the capacitance matrix

Appendix B: Experimental data

B.1 Vector Network Analyser results

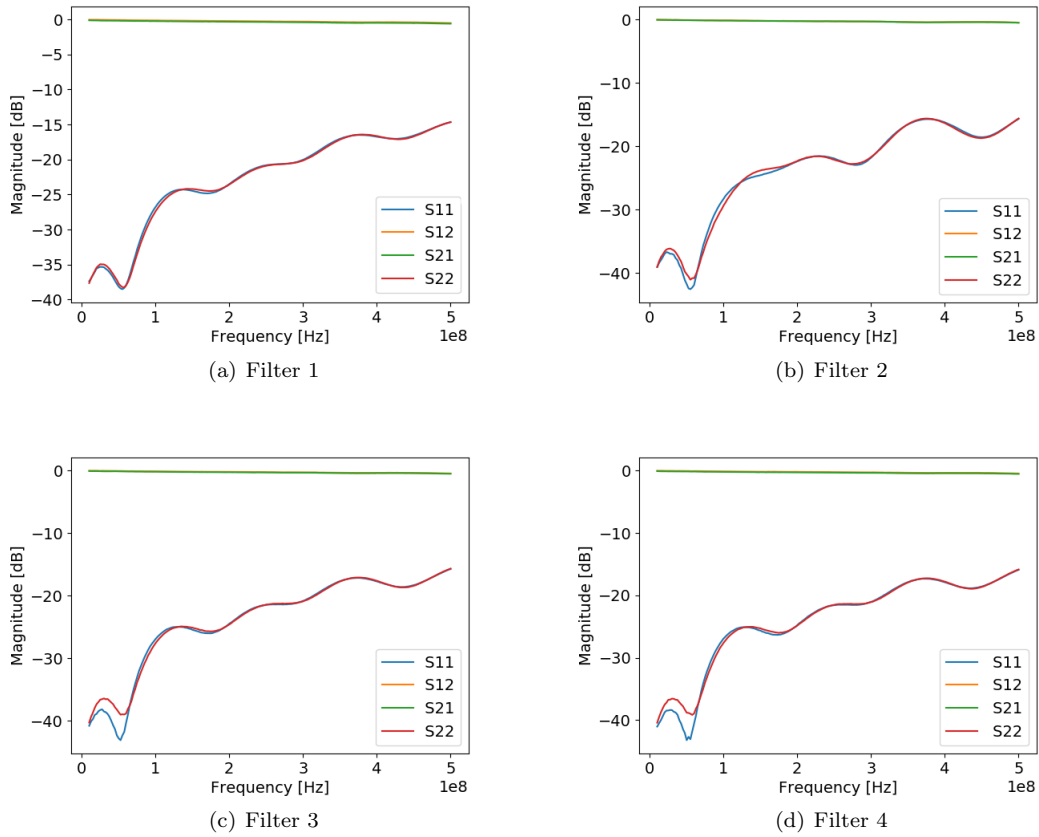


Figure 8: Transmission and reflection parameters of 4 filters measured with a VNA. The lines representing S12 (yellow) and S21 (green) are superposed, and the same happens for S11 (blue) and S22 (red).

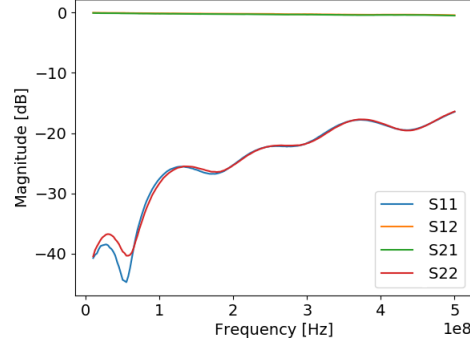


Figure 9: Transmission and reflection parameters of Filter 5 measured with a VNA. The lines representing S12 (yellow) and S21 (green) are superposed, and the same happens for S11 (blue) and S22 (red).

B.2 Terahertz time-domain spectrometer results

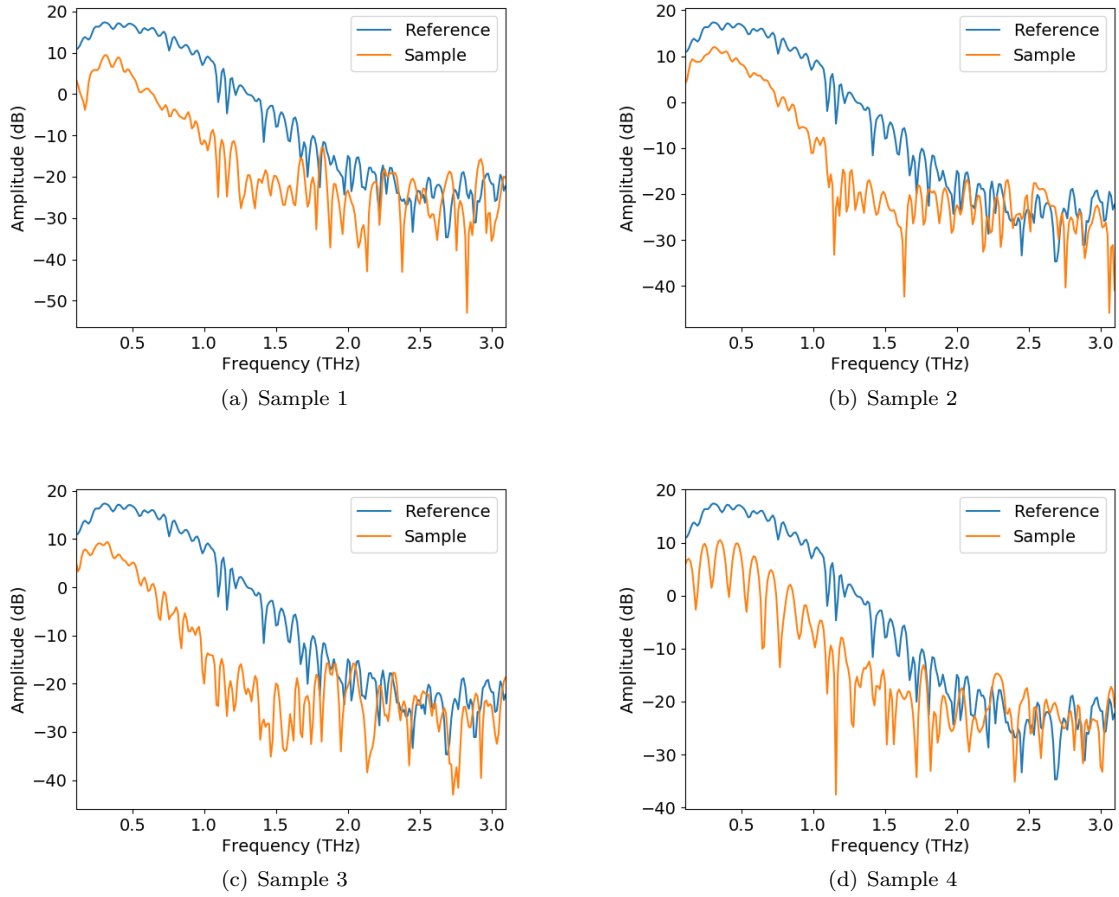
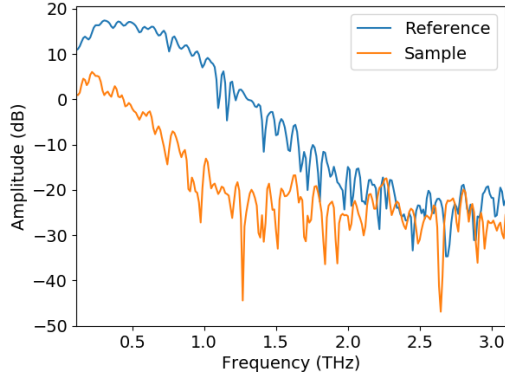
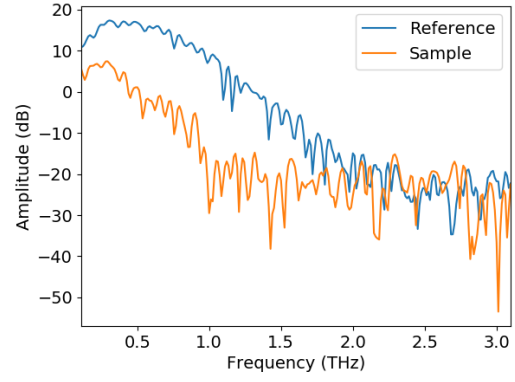


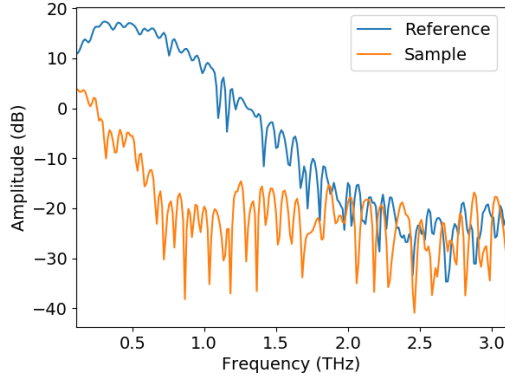
Figure 10: Measurements made using the terahertz spectrometer. The results from samples 1 to 4 are compared with the reference curve of the instrument. The numeration of the samples is explained in Table 4.1



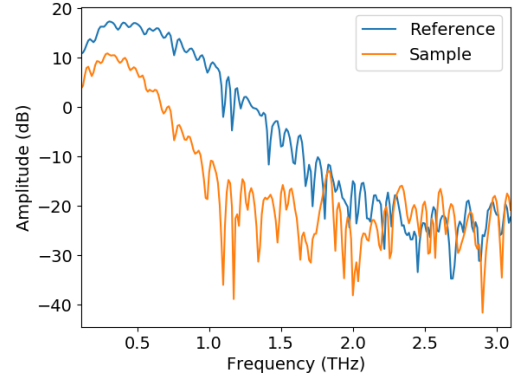
(a) Sample 5



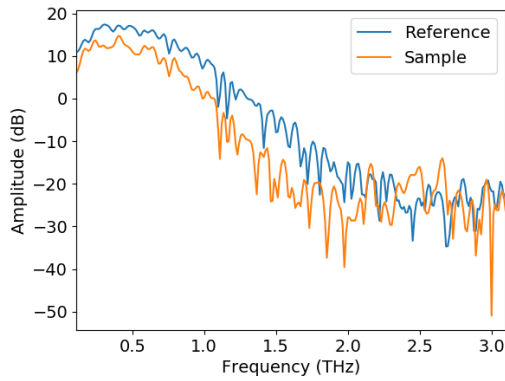
(b) Sample 6



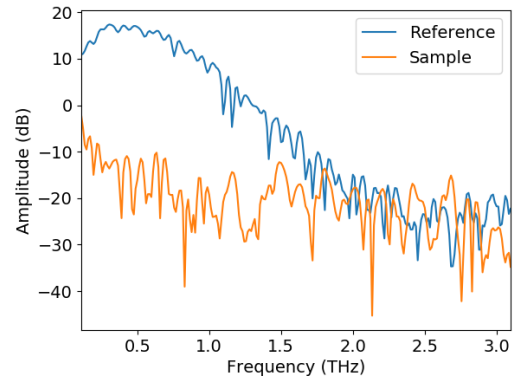
(c) Sample 7



(d) Sample 8

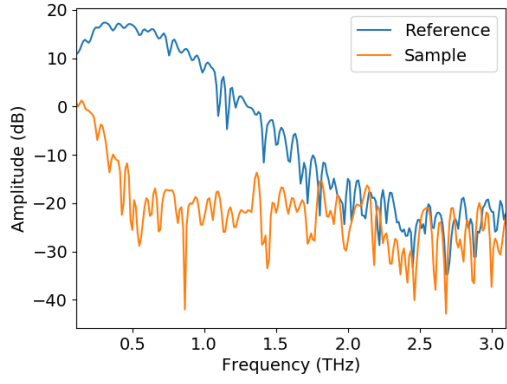


(e) Sample 9

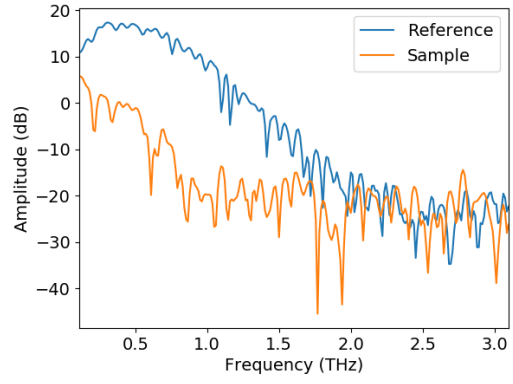


(f) Sample 10

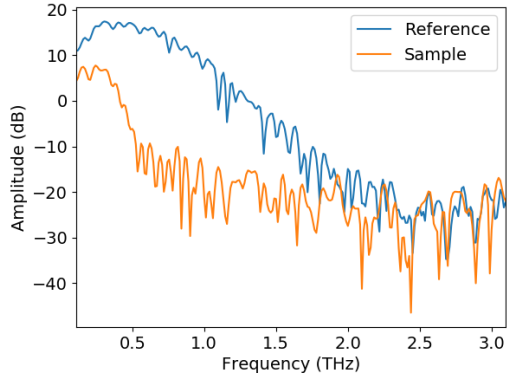
Figure 11: Measurements made using the terahertz spectrometer. The results from samples 5 to 10 are compared with the reference curve of the instrument. The numeration of the samples is explained in Table 4.1



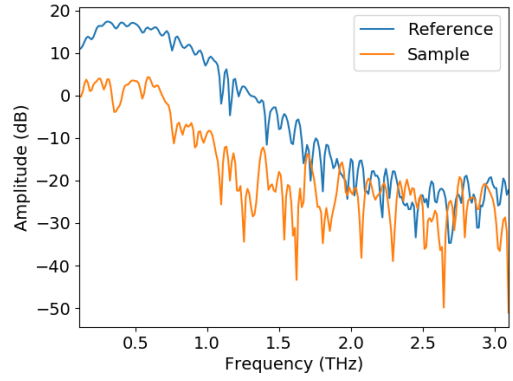
(a) Sample 11



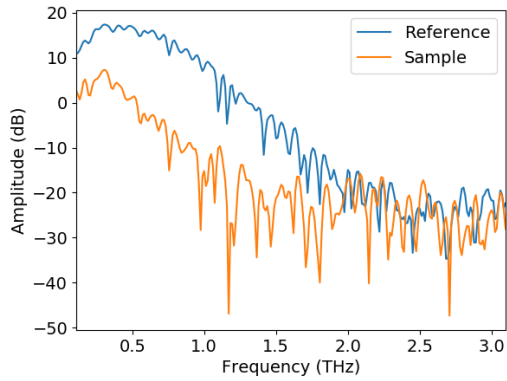
(b) Sample 12



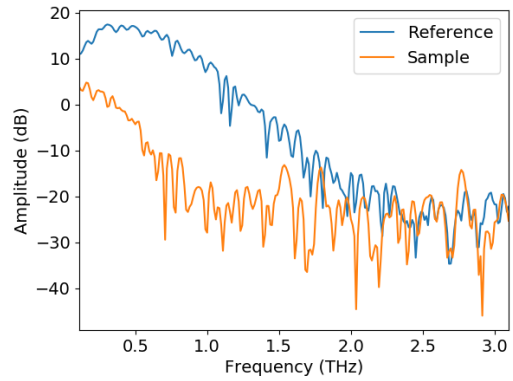
(c) Sample 13



(d) Sample 14

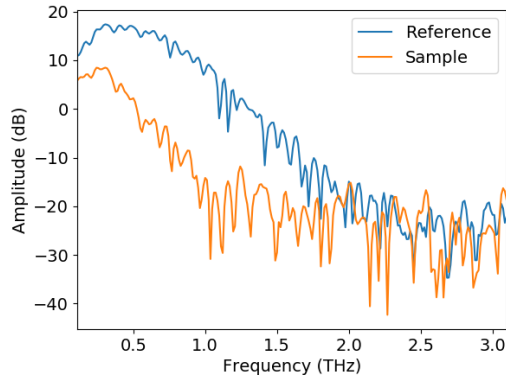


(e) Sample 15

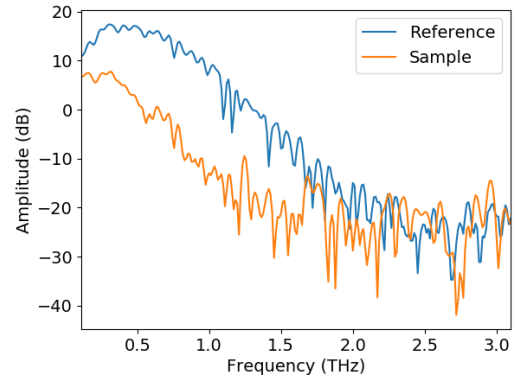


(f) Sample 16

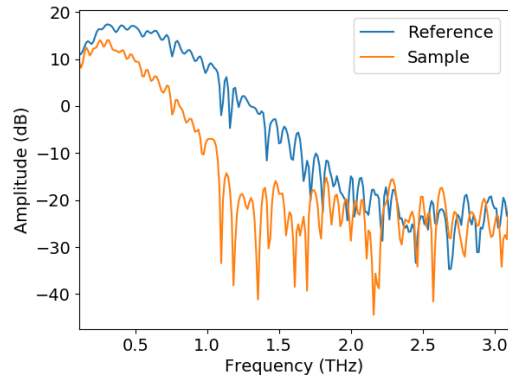
Figure 12: Measurements made using the terahertz spectrometer. The results from samples 11 to 16 are compared with the reference curve of the instrument. The numeration of the samples is explained in Table 4.1



(a) Sample 17



(b) Sample 18



(c) Sample 19

Figure 13: Measurements made using the terahertz spectrometer. The results from samples 17 to 19 are compared with the reference curve of the instrument. The numeration of the samples is explained in Table 4.1